

T-FAKE: Synthesizing Thermal Images for Facial Landmarking

Philipp Flotho*
Saarland University

Moritz Piening*
Technical University of Berlin

Anna Kukleva
MPI for Informatics, SIC

Gabriele Steidl
Technical University of Berlin

Abstract

Facial analysis is a key component in a wide range of applications such as healthcare, autonomous driving, and entertainment. Despite the availability of various facial RGB datasets, the thermal modality, which plays a crucial role in life sciences, medicine, and biometrics, has been largely overlooked. To address this gap, we introduce the T-FAKE dataset, a new large-scale synthetic thermal dataset with sparse and dense landmarks. To facilitate the creation of the dataset, we propose a novel RGB2Thermal loss function, which enables the domain-adaptive transfer of RGB faces to thermal style. By utilizing the Wasserstein distance between thermal and RGB patches and the statistical analysis of clinical temperature distributions on faces, we ensure that the generated thermal images closely resemble real samples. Using RGB2Thermal style transfer based on our RGB2Thermal loss function, we create the large-scale synthetic thermal T-FAKE dataset[†] with landmark and segmentation annotations. Leveraging our novel T-FAKE dataset, probabilistic landmark prediction, and label adaptation networks, we demonstrate significant improvements in landmark detection methods on thermal images across different landmark conventions. Our models show excellent performance with both sparse 70-point landmarks and dense 478-point landmark annotations. Moreover, our RGB2Thermal loss leads to notable results in terms of perceptual evaluation and temperature prediction.

1. Introduction

Functional thermal imaging is an acquisition modality with growing importance in many areas from life sciences over medicine to biometrics. Due to the close relation of body temperature with physiological states, thermal imaging of faces emerged as an important tool for screening infectious diseases [4, 45, 53] and for the analysis of neurocognitive and affective states [24]. As a consequence, there exists a growing need for thermal images with annotated facial landmarks. However, in contrast to RGB images, annotated data for thermal images of faces is still rarely available. For example, the largest thermal datasets with facial

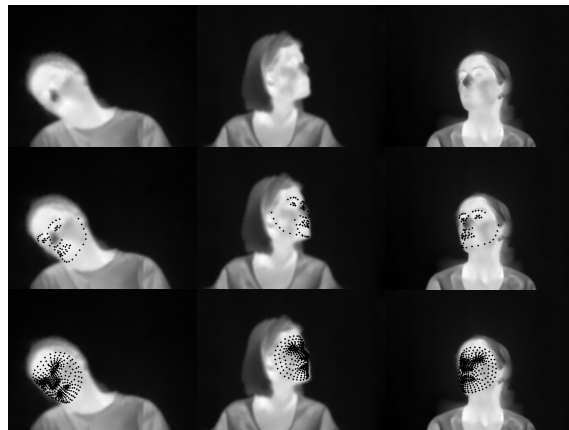


Figure 1. Predictions of 70 (middle) and 478 (bottom) point facial landmarks on the challenging CHARLOTTE dataset which are estimated accurately by training a model with our synthetic data.

landmark annotations contain only tens to hundreds of individuals [3, 13, 33, 51], while the largest datasets for face detection for RGB images reached the mark of a million faces (of more than 500k individuals) with the MegaFace benchmark already in 2016 [28]. Moreover, large synthetic RGB datasets, like FAKE [60], appeared to be valuable for sparse and dense landmark detection training. Generally, the detection of facial landmarks is an important task for further facial analysis. These 2D coordinates of corresponding points across faces are relevant for, e.g., face alignment [61], animation of 3D avatars [39], motion magnification [14, 15] or deepfakes [54]. The most common convention for facial landmark annotations uses 68 points across the face and face boundary [57]. Even though the 68-point convention remains challenging for thermal images [41, 50], there is additional demand for dense landmarks with more than 300 points. [39, 60, 61].

Faces in thermal images share structural similarities with RGB images. However, temporally varying environmental factors such as temperature and rain droplets, and physiological factors such as blood perfusion changes and vascular details lead to much higher variability in the appearance of faces within individuals [21]. Sweating, flushing, or outdoor rain can result in time-dependent texture changes. Features that are very stable in RGB images such

*Equal Contribution; [†]<https://github.com/phfloth/tfake>

as the contrast of the nose and the eyes can become inverted when the nose or the face is cooled down. Thus, RGB landmarks display decent results on thermal images [13], but show high failure rates and imprecise landmark predictions on challenging thermal images. Up to now, there exist only a few sparse thermal landmark detection methods [33, 36, 37, 41, 51], and we are unaware of dense thermal or a multimodal RGB+Thermal landmarks.

In this paper, we aim to address this gap by introducing the T-FAKE dataset, the first large-scale synthetic thermal dataset featuring both sparse and dense landmarks for facial analysis. We propose to thermalize a synthetic RGB dataset using our novel RGB2Thermal loss function, which comprises three key components: i) a supervised data term that controls the generation of thermal faces based on a small subset of RGB-thermal pairs, ii) a Wasserstein distance term that aligns the patch distributions of the generated synthetic thermal images with those of real thermal images, and iii) a term incorporating prior information on clinical temperature statistics for different facial regions. This loss enables our model to generalize beyond available lab-condition data to ‘in-the-wild’ images. Figure 2 shows T-FAKE samples and illustrates the advantage of our semi-supervised model over a supervised model trained solely with lab-condition images. To validate the quality of our T-FAKE dataset, we employ a probabilistic landmark prediction method with integrated face detection by minimizing the negative log-likelihood function of the landmarks which are assumed to follow a Gaussian distribution as proposed in [61]. Moreover, by introducing a learnable adapter between different landmark conventions, we unify various methods and datasets for evaluation.

We thoroughly evaluate the landmark prediction method trained on our T-FAKE dataset on the challenging thermal dataset CHARLOTTE [3], which includes controlled modulation of temperature, pose, and resolution and on the established RGB dataset 300W [57]. Our model demonstrates superior performance on the thermal landmark prediction benchmark compared to previous methods while maintaining performance on RGB images comparable to state-of-the-art RGB methods. Figure 1 illustrates the performance of our model for sparse and dense landmarking.

In summary, we provide the following contributions:

- The first large-scale facial synthetic thermal dataset T-FAKE with 70 sparse and 478 dense landmarks and additional semantic segmentation masks;
- A novel RGB2Thermal loss to facilitate thermal image synthesis overcoming lab-recorded training data with limited image variability;
- Training of the up-to-date first dense thermal landmarker and a state-of-the-art multimodal RGB+Thermal sparse landmarker in combination with highly structured benchmarking across landmark conventions and modalities.



Figure 2. Challenging frames from the FAKE dataset [60] before (first row) and after thermalization without any regularization (second row) and our domain-adaptive model (third row). Thermalized backgrounds are removed based on given segmentation. The last row displays the segmentation masks with gray levels which are proportional to the reference temperature values used in regularizer (3). The first three images exemplify the ‘cold’ setup with colder noses and the last two the ‘warm’ setup with warmer noses.

2. Related Work

Facial RGB landmarking. Different annotation conventions exist for labeled landmarking datasets. An important distinction is between 2D annotations and 3DA-2D annotations which project 3D landmarks onto images [11]. 2D is closer to human perception, but 3DA-2D enables annotation of occluded face regions. The most widely used annotation convention defines 68-point 2D landmarks available for many facial alignment datasets [6, 18, 31, 66]. Sometimes points on the eye or other details are additionally added [3, 60]. While an in-depth review of facial RGB landmarking is beyond the scope of this work, we introduce those that are relevant to thermal landmarking methods. Kazemi et al. [27] introduced a popular traditional computer vision method for landmark prediction via the dlib library [29]. Kowalski et al. [34] proposed the deep alignment network (DAN) which uses convolutional neural networks and iteratively refines predictions. Around the same time, Bulat et al. [6] proposed the facial alignment network (FA). Both methods predict heat maps of landmark positions. Explicit integration of uncertainty quantification into a landmark prediction model via the LUVLi loss has been proposed by Kumar et al. [35]. Recently, image annotation quality became a limiting factor which led to the emergence of synthetic data with high-quality ground truth [43]. Wood et al. [60, 61] trained 3DA-2D landmarkers with excellent performance using their proposed synthetic FAKE dataset with 100k frames of at least 2k individuals. Note that most landmarkers are trained on facial bounding boxes. As a result,

they are either evaluated in combination with a face detector or on pre-defined ground truth bounding boxes. Here, we focus on the combined evaluation of face and landmark detection, a harder, but more practical task.

Thermal landmarking. Many tailored approaches for thermal landmarking use similar architectures as RGB landmarkers and are mainly developed alongside the publication of new datasets, see Table 1. Kuzdeuov et al. [36] released the TFW dataset with 5 facial landmarks and bounding boxes and trained YOLOv5 networks for landmark prediction. The SF-TL54 dataset [37] has been used for 2D landmark prediction with a dlib and a U-net model. Kopaczka et al. [33] use a DAN for their AACHEN dataset with 68-point 2D landmarks. A highly structured 2D landmarking dataset is the CHARLOTTE thermal face dataset with controlled temperature changes by Ashrafi et al [3]. It contains around 10k images in total and 7684 images with annotations. In contrast to these publicly available datasets, datasets with limited or no public availability include the the ARL-VTF dataset [51] and a dataset recorded in SARS-CoV-2 drive-in stations (DRIVE-IN) [13] (six minutes recordings at 50Hz of 436 subjects). The authors of the DRIVE-IN dataset found that a stack of pre-processing functions already leads to a good performance of existing RGB landmark models on thermal images. Note that such thermal datasets are often captured with uncooled microbolometers with automatic radiometric calibration. This leads to comparable temperature values but may introduce small measurement errors. Beyond thermal images, Poster et al. [52] proposed to use transfer learning on a siamese DAN to improve thermal landmark prediction with RGB facial landmarks. Mallat et al. [41] used RGB2Thermal image translation (‘thermalization’), active appearance models, and deep alignment networks of RGB datasets for thermal landmark prediction. In contrast to the previous work, our dataset contains thermal images of at least 2k individuals that are annotated with sparse 70 3DA-2D and dense 478 2D point landmarks.

Thermalization. In addition to thermal landmark datasets, various datasets of paired and aligned thermal and RGB images without annotations exist. These can be employed for the training of thermalization models. In contrast to the rich literature on Thermal2RGB synthesis [44, 55, 63], the literature on RGB2Thermal image synthesis using such datasets is more limited. Mallat et al. thermalized facial images by minimizing a perceptual loss [41] using the VIS-TH dataset [40]. Similarly, generative adversarial networks (GANs) have been used for Thermal2RGB synthesis [21, 62] using the NCKU-VTF [21] dataset and the ARL-MMDF [62] dataset containing facial image data. In contrast to the limited public availability of these two datasets, a publicly available dataset with paired facial images is the multimodal disguise *Sejong face database* (SEJONG) with 100 subjects, 15 disguise variations and 4849 RGB+Thermal

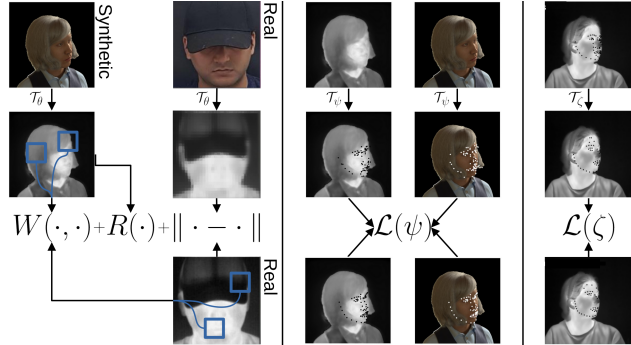


Figure 3. Three steps of our training pipeline (models and their loss functions): 1. thermalization network \mathcal{T}_θ with loss (1) - (3). 2. landmark prediction network \mathcal{T}_ψ with (10). 3. landmark adaptation network \mathcal{T}_ζ with (11). We show black dots for thermal landmarks and white dots for RGB landmarks. Note the landmark adaptation on the forehead in the last step.

image pairs by Cheema and Moon [7]. Note that all these datasets and resulting models are mostly restricted to frontal views of faces with controlled lighting. Thermalization of general scenes has been achieved by Kniaz et al. [30] with a modified Pix2Pix GAN based on the 5098 triplets of RGB images, thermal images, and segmentation masks in the ThermalWorld dataset. In contrast to previous works, we employ a semi-supervised RGB2Thermal loss using a semantic segmentation to improve generalization beyond lab-condition frontal views to ‘in-the-wild’ images.

3. T-FAKE Dataset

Recently, the success of facial landmarkers trained solely on the FAKE dataset [60], a synthetic facial landmarking dataset, has demonstrated the potential of synthetic data for the task. We aim to transfer this success story to the largely overlooked thermal domain and the multimodal setting by introducing our synthetic thermal landmarking dataset T-FAKE featuring at least 2k unique subjects. In particular, we train a semi-supervised image translation model for the thermalization of RGB images using real and synthetic data. To account for data variations in terms of poses, shadows, and expressions, we employ a semi-supervised loss.

3.1. Thermalization

To generate our large-scale synthetic T-FAKE dataset, we propose a thermalization framework (see Figure 3). First, we train our network in a semi-supervised manner based on training pairs of RGB+Thermal images $(\mathbf{X}_{\text{RGB}}, \mathbf{X}_{\text{T}}) = (X_{\text{RGB}}^n, X_{\text{T}}^n)_{n=1}^N$ from the lab-recorded SEJONG dataset. Further, we use the synthetic RGB images from FAKE $\mathbf{X}_{\text{FAKE}} = (X_{\text{FAKE}}^m)_{m=1}^M$ for which no thermal counterpart exists. The thermalization of these data appears to be difficult due to the large differences between real-world lab-recorded and synthetic in-the-wild data when facing ther-

Dataset Name	Year	DS Available	Model Available	Landmarks	Size (F/S)	Distance (cm)	Out-of-Lab
Aachen [33]	2018	✓	✓	68	2935/90	90	✗
ARL-MMFD [62]	2019	(request)	✗	6	888/111	250, 500, 750	✗
DRIVE-IN [13]	2021	✗	✗	68 and 478	~7-8M/436	~80-150	✓
ARL-VTF [51]	2021	✗*	✗	6	500k/395	210	✗
TFW [36]	2022	✓	✓	5	9982/147	≥100	✓
SF-TL54 [37]	2022	✓	✓	54	2556/142	100	✗
CHARLOTTE [3]	2022	✓	✗	72 (43 profile)	7684/10	100-660	✗
T-FAKE (ours)	2024	✓	✓	70 and 478	200k/≥2k	~80-150	✓

Table 1. Thermal landmark dataset comparison. Indicated are the number of frames (F) and subjects (S), camera distance, and if recorded outside of a controlled laboratory. Unavailable data are marked by ✗ and ✗* indicates no response received from corresponding authors.

malization tasks. For RGB2Thermal translation, we optimize a U-net [56] T_θ by minimizing the loss function

$$\mathcal{L}(\theta) := \frac{1}{N} \sum_{n=1}^N \|T_\theta(X_{\text{RGB}}^n) - X_{\text{T}}^n\|_2^2 \quad (1)$$

$$+ \lambda_W W(T_\theta(\mathbf{X}_{\text{FAKE}}), \mathbf{X}_{\text{T}}) \quad (2)$$

$$+ \lambda_R \frac{1}{M} \sum_{m=1}^M R(T_\theta(X_{\text{FAKE}}^m)), \quad \lambda_W, \lambda_R > 0. \quad (3)$$

This loss allows us to train a supervised image translation model from paired data while ensuring domain-generalization of the model using unpaired data. The first summand (1) penalizes the deviation of the generated thermal image from the true one and serves as a reconstruction loss for known image pairs. The second summand (2) exploits the Wasserstein distance on the patch distribution of thermalized FAKE images and natural thermal images. This style loss ensures that a generated image displays the thermal image statistics. To be more precise, recall that the squared Wasserstein-2 distance \mathcal{W}_2^2 between empirical measures $\mu = \frac{1}{K} \sum_{k=1}^K \delta_{x_k}$ and $\nu = \frac{1}{L} \sum_{l=1}^L \delta_{y_l}$ for Dirac probability measures δ_\bullet is given by

$$\mathcal{W}_2^2(\mu, \nu) := \inf_{\pi \in \Pi} F(\pi) := \inf_{\pi \in \Pi} \sum_{k=1}^K \sum_{l=1}^L \|x_k - y_l\|^2 \pi_{k,l}, \quad (4)$$

where Π denotes the set of non-negative $K \times L$ matrices which rows and columns sum up to $1/K$ and $1/L$, respectively. Calculation with this distance requires solving costly optimization problems. As a remedy, the entropy-regularized Wasserstein distance

$$\mathcal{W}_{2,E}^2(\mu, \nu) := \inf_{\pi \in \Pi} \left\{ F(\pi) + \lambda_E \sum_{k=1}^K \sum_{l=1}^L \pi_{k,l} \log(\pi_{k,l}) \right\} \quad (5)$$

with some (small) regularization $\lambda_E > 0$ has been proposed [9]. This term and its gradients can efficiently be calculated via the Sinkhorn algorithm [12, 49]. To use this loss for thermal translation, we focus on the (subsampling) patch

distributions of the generated and real images. For that purpose, we now extract (overlapping) image patches by defining the patch extractor $P_i X := X[i_1 : i_1+s, i_2 : i_2+s]$, $i = (i_1, i_2) \in I$ of size $s \times s$ and considering the empirical measures generated by the patch distributions of $T_\theta(\mathbf{X}_{\text{FAKE}})$,

$$\mu_{\text{FAKE}} := \frac{1}{M} \frac{1}{|I|} \sum_{m=1}^M \sum_{i=1}^{|I|} \delta_{P_i(T_\theta(X_{\text{FAKE}}^m))}, \quad (6)$$

and similarly μ_{T} from X_{T} . Now we penalize in (2) the term

$$W(T_\theta(\mathbf{X}_{\text{FAKE}}), \mathbf{X}_{\text{T}}) := \mathcal{W}_{2,E}^2(\mu_{\text{FAKE}}, \mu_{\text{T}}). \quad (7)$$

During training, we apply a *multiscale approach* by applying this regularizer over multiple image scales and summing over the results. As a result, the patch statistics of down-scaled images are incorporated into the empirical loss. The proposed patch distribution matching-based regularization was inspired by its application in related tasks such as image reconstruction [1, 49], style transfer [38], texture reconstruction [2, 19], and image translation [25].

Finally, the distribution of temperature across different regions of the face and body are well-studied [8, 59], e.g., warmer areas around the eyes, colder scalp hair and glasses blocking thermal heat. Thus, the third summand (3) incorporates such knowledge about the expected temperature in different facial areas. To be specific, we make use of a given semantic segmentation of the synthetic dataset of the image $\mathbf{X}_{\text{F-RGB}}$ into pixels corresponding to 18 regions S_i , e.g., ‘background’, ‘nose’, ‘headwear’ and so on. Moreover, let T_i be the average temperature of the hardcoded reference temperatures in the region S_i based on measurements presented in empirical studies [3, 8, 59]. Then, we compute

$$R(T_\theta(\mathbf{X}_{\text{FAKE}})) = \sum_{m=1}^M \sum_{i=1}^{18} \omega_i (\overline{S_i(T_\theta(X_{\text{FAKE}}^m))} - T_i)^2, \quad (8)$$

where the weights ω_i are proportional to the region sizes and $\overline{S_i}$ is the mean temperature in the i -th region. Note that facial temperatures depend on the environmental conditions. Hence, we train T_θ two times with two different ref-

erence temperature sets to simulate ‘cold’ and ‘warm’ environmental conditions. The segmentations are shown in Figure 2 (bottom) and different regularizers in Figure 3 (left).

Predictions of the normalized temperature with our model compared to a model without regularization are shown in Figure 2. The advantages of our regularization in a domain-adapted setting are clearly visible. The use of regularization reduces image artifacts. The patch regularizer (2) promotes natural texture synthesis and because of our segmentation regularizer (3) temperature differences between facial areas are more pronounced. Hence, our method allows for the adaptation of images with shadows, various skin colors, and distinctive facial expressions. In particular, such features may be underrepresented in facial thermal imaging datasets recorded in lab conditions. Note that the resulting domain adaptation needs for synthetic data solved by a semi-supervised approach based on the access to ground truth segmentations differentiates our task from the RGB2Thermal tasks in [30, 41] and (supervised) Thermal2RGB tasks in [21, 44, 63]. Generalization limitations of supervised models are discussed in the supplementary.

3.2. The Dataset

Having trained T_θ , we use it to thermalize the FAKE dataset which results in the thermal dataset T-FAKE. For each thermal condition, the dataset contains 100k images featuring at least 2k unique subjects. Each image is available in a simulated ‘cold’ and a ‘warm’ environment adding up to 200k images. This number of frames and subjects surpasses the numbers in other thermal landmarking datasets [3, 13, 33, 36, 37, 51, 62] known to the authors. In contrast to thermal landmarking datasets with a fixed distance between the subjects and the camera [33, 37, 51], the distance varies within an estimated range of 80cm to 150cm for the T-FAKE dataset. Moreover, the synthesized images are based on facial scans with a wide range of age and ethnicity and a balanced number of people identifying as male or female [60]. In addition to the original ground truth sparse 3DA-2D landmark annotations, we add dense 2D annotations by transferring Mediapipe [39] predictions for the FAKE to the T-FAKE dataset. This makes our dataset the first densely annotated thermal landmarking dataset. While we found many large thermal landmarking datasets to be non-public [13, 51, 62], our complete dataset with both thermal conditions and annotations is available for download. In combination with the original FAKE dataset, we can train multimodal facial landmarkers jointly on RGB and thermal images as described in the next section. Table 1 displays a comparison between thermal landmarking datasets.

4. Facial Landmarking

Learning with synthetic images has proven to be very useful in facial landmarking [60–62]. Based on the proposed T-

FAKE and the original FAKE dataset, we can train a supervised thermal or multimodal landmark prediction model for thermal and RGB images using synthetic data only. Moreover, we adapt a model to new annotation conventions by training a small-scale label adaptation model. The data flow for these models is visualized in Figure 3.

4.1. Landmark Prediction

We apply the construction in [61] and learn a landmark prediction model through probabilistic landmark regression from given paired data $(X^j, \mathbf{y}_j)_{j=1}^J$, where $X^j \in \text{FAKE} \cup \text{T-FAKE}$ and $\mathbf{y}_j := (y_l^j)_{l=1}^L, y_l^j \in \mathbb{R}^2$ are the corresponding L landmarks. We learn a network T_ψ mapping from the space of images to the space of L -fold two-dimensional Gaussian distributions $(\mathcal{N}(\mu_l, \sigma_l I_2))_{l=1}^L$. Here we employ a MobileNet V2 architecture for landmark prediction [58]. Recalling that the Gaussian distribution $\mathcal{N}(\mu, \sigma I_2)$ has the *negative log-likelihood function*

$$-\log p(y|\mu, \sigma) = \log(2\pi\sigma^2) + \frac{\|\mu - y\|_2^2}{2\sigma^2}, \quad (9)$$

the authors of [61] proposed to learn the network $T_\psi := (T_\psi^1, T_\psi^2)$ with $X \mapsto (\boldsymbol{\mu}, \boldsymbol{\sigma}^2)$, where $\boldsymbol{\mu} = (\mu_l)_{l=1}^L \in (\mathbb{R}^2)^L$ and $\boldsymbol{\sigma}^2 = (\sigma_l^2)_{l=1}^L \in \mathbb{R}^L$ by minimizing the loss function

$$\mathcal{L}(\psi) := \sum_{l=1}^L \left(\sum_{j=1}^J \log T_{\psi,l}^2(X^j) + \frac{\|T_{\psi,l}^1(X^j) - y_l^j\|_2^2}{2T_{\psi,l}^2(X^j)} \right). \quad (10)$$

During training, we clip $T_{\psi,l}^2 \geq \varepsilon > 0$ to avoid numerical instability due to too small variances. The first sum controls the location accuracy and the second one the uncertainty prediction. Having learned the network T_ψ , it produces not only the expected values $\boldsymbol{\mu}$ of the landmarks, but also a measure for its uncertainty $\boldsymbol{\sigma}^2$. We threshold the average uncertainty score of multiple sliding windows to enable face detection in our implementation and refer to this as Gaussian log-likelihood with sliding windows (**GLL+SW**).

4.2. Label Adaptation

A common evaluation approach that is especially crucial for synthetic data and comparison of 2D and 3DA-2D landmarks is label adaptation [60, 61]. It allows us to adapt to different landmark conventions between the training dataset and an evaluation dataset. Given two sequences $(\hat{\mathbf{y}}_k, \mathbf{y}_k)_{k=1}^K$ with predicted landmarks $\hat{\mathbf{y}}_k := (\hat{y}_l^k)_{l=1}^{\hat{L}} \in \mathbb{R}^{2\hat{L}}$, and with ground truth landmarks $\mathbf{y}_k := (y_l^k)_{l=1}^L \in \mathbb{R}^{2L}$ with possibly $\hat{L} \neq L$, we aim to train a third label adaptation model $T_\zeta : \mathbb{R}^{2\hat{L}} \rightarrow \mathbb{R}^{2L}$. Here, we use the loss

$$\mathcal{L}(\zeta) = \frac{1}{K} \sum_{k=1}^K \|T_\zeta(\hat{\mathbf{y}}_k) - \mathbf{y}_k\|_1. \quad (11)$$

Since we deal with low-dimensional data, we use a simple multi-layer fully connected perceptron with 5 layers for this task, see supplementary material for details.

5. Experiments

We experimentally evaluate our T-FAKE dataset and the underlying model. Firstly, we assess the quality of an RGB+Thermal landmarker with integrated face detection trained on FAKE+T-FAKE in comparison to available pre-trained thermal landmarkers and state-of-the-art RGB landmarkers. Secondly, we quantify the perceptual T-FAKE quality based on an unsupervised metric. Thirdly, we report the temperature prediction performance of the underlying model using the mean-squared error (MSE). Note that we clamp the temperature of all thermal images between 20 °C and 40 °C for all experiments and visualizations.

5.1. Implementation Details

Thermalization. We train on the RGB+Thermal SEJONG dataset recorded in lab conditions and the large-scale synthetic FAKE dataset featuring in-the-wild RGB images. We train on a resolution of 256×256 . The resolution-agnostic U-net allows to apply our two models trained on 256×256 images to the FAKE dataset at the original 512×512 resolution to generate the T-FAKE dataset. This results in the up-to-date largest thermal landmarking dataset with 200k images of at least 2k unique subjects and two thermal settings, see Table 1. We refer to the supplementary for details.

Face-Detection+Landmarker. We simultaneously train our landmark prediction model using a sparse 70-point 3DA-2D and dense 478-point 2D landmark convention with an image size of 224×224 on our new T-FAKE thermal dataset and the original FAKE RGB dataset. Additionally, we mix texture images with random landmarks as negative samples into the training to create meaningful uncertainty estimates σ_l . Due to the limited, public availability of the dense 3DA-2D ground truth in the FAKE dataset [60], we use the 478-point 2D predictions of the MediaPipe model for the synthetic RGB images as our dense ground truth dense annotations.

During inference, we use a multi-scale sliding window evaluation to generalize our model to varying image sizes without direct face tracking beyond pre-defined bounding boxes. For our final landmark prediction, we pool all predictions and use the window with the smallest average standard deviation across all scales and all sliding windows. To integrate face detection into the model, we use the average $\bar{\sigma}$ of the landmark uncertainties σ_l , $1 \leq l \leq L$ of the final window per frame and detect faces only if $\bar{\sigma}$ is less than a fixed threshold t , i.e., GLL+SW ($\bar{\sigma} < t$). Hence, $\bar{\sigma} < \infty$ corresponds to evaluation on all frames. We refer to the supplementary for more details.

Label Adaptation. Our label adaptation network is trained

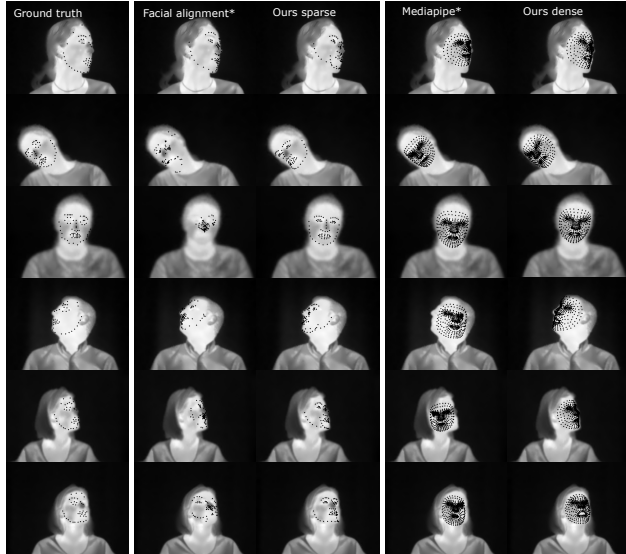


Figure 4. CHARLOTTE [3] examples using FA and Mediapipe with pre-processing stack and our models without label adaptation. While RGB methods can handle some challenging poses, they may produce broken landmarks on difficult images.

solely on the two-dimensional landmark predictions and ground truth annotations of our random training split of a benchmark dataset and not on the images. This dataset is later excluded from the final evaluation. We do not use the predicted standard deviation at this stage. Again, we use random rotations and shear transformations during training.

Evaluation Metrics for Landmarking. We report the *normalized mean error* (NME) [57, 60, 67] for evaluation, i.e., the mean absolute error (MAE) normalized with an image-dependent constant to account for varying image sizes. Often, normalization is performed by the distance between the outermost eye landmarks (NME IO) [57, 60]. However, the CHARLOTTE benchmark dataset contains many examples with side profile views where only one of the eyes is visible. Therefore, we use the average height and width of the bounding box around the face for normalization [67] (NME W/H). Apart from the NME, we report the failure rates for each of the reference methods. The failure rate is the percentage of frames where no faces could be found. Frames without recognized faces are not included nor weighted in the NMEs. The method of rejection varies for each landmarker. We use vanilla parameters except for MediaPipe [39], where we set the minimal detection confidence to 0.01. We report T-FAKE landmarker results for different levels of face detection confidence to illustrate the trade-off between failure rate and NME.

5.2. Benchmark Datasets for Landmarking

To compare thermal performance, we use the CHARLOTTE dataset due to its high variability in resolution,

Metric	Method	Training Dataset	High	Low	Side	Front	Full
NME W/H ↓	3FabRec [5]	300W [†]	0.0931	0.1084	0.0675	0.1344	0.1009
	3FabRec*	300W [†]	0.0814	0.1558	0.0791	0.1602	0.1196
	Star [64]	300W [†]	0.0707	0.1021	0.0673	0.1064	0.0868
	Star*	300W [†]	0.0639	0.1273	0.0703	0.1227	0.0965
	Mediapipe [39]	<i>undisclosed</i> [†]	0.1900	0.2745	0.2879	0.1865	0.2262
	Mediapipe*	<i>undisclosed</i> [†]	0.1400	0.2621	0.1838	0.2164	0.2023
	FA [6]	LS3D-W [†]	0.1070	0.2790	0.1222	0.2508	0.1875
	FA*	LS3D-W [†]	0.1007	0.2207	0.1075	0.2123	0.1593
	DAN [32]	AACHEN	0.1677	0.2405	0.2942	0.1731	0.2054
	YOLO5Face [36]	TFW	0.0787	0.1249	0.0701	0.1311	0.1012
	U-Net+Wing [37]	SF-TL54	0.2476	0.3134	0.1757	0.3596	0.2829
	Dlib [37]	SF-TL54	0.2159	0.2174	0.1365	0.2741	0.2167
	GLL+SW ($\bar{\sigma} < \infty$) [60, 61]	FAKE [†]	0.1055	0.2675	0.1241	0.2534	0.1887
	GLL+SW* ($\bar{\sigma} < \infty$)	FAKE [†]	0.0933	0.2682	0.1312	0.2348	0.1824
	GLL+SW Dense ($\bar{\sigma} < \infty$)	FAKE [†] + T-FAKE	0.0854	0.1395	0.0764	0.1500	0.1132
	GLL+SW Sparse ($\bar{\sigma} < \infty$)	FAKE [†] + T-FAKE	0.0683	0.1239	0.0645	0.1294	0.0969
	GLL+SW Sparse ($\bar{\sigma} < 6 \times 10^{-4}$)	FAKE [†] + T-FAKE	0.0671	0.1118	0.0593	0.1179	0.0889
GLL+SW Sparse ($\bar{\sigma} < 2.2 \times 10^{-4}$)	FAKE [†] + T-FAKE	0.0661	0.1018	0.0551	0.1059	0.0815	
Failure rate (%) ↓	Mediapipe [39]	<i>undisclosed</i> [†]	25.05	46.85	50.09	22.40	36.25
	Mediapipe*	<i>undisclosed</i> [†]	12.80	14.07	24.97	1.92	13.45
	FA [6]	LS3D-W [†]	12.95	27.43	21.71	19.07	20.39
	FA*	LS3D-W [†]	0.83	10.45	4.75	6.80	5.77
	DAN [33]	AACHEN	49.32	48.72	72.85	25.15	49.01
	YOLO5Face [36]	TFW	13.14	21.55	19.26	15.66	17.46
	U-Net+Wing / Dlib [37]	SF-TL54	29.29	22.57	38.16	13.50	25.84
	GLL+SW ($\bar{\sigma} < 6 \times 10^{-4}$)	FAKE [†] + T-FAKE	0.98	10.34	6.94	4.64	5.79
	GLL+SW ($\bar{\sigma} < 2.2 \times 10^{-4}$)	FAKE [†] + T-FAKE	6.52	32.76	23.33	16.68	20.00

Table 2. Results on CHARLOTTE dataset splits. The pre-processing stack for RGB landmarks [13] is indicated by *. Best NME value is in bold. Failure rate of GLL+SW depends on the freely chosen confidence threshold $\bar{\sigma}$. We include all predictions for $\bar{\sigma} < \infty$, Star and 3FabRec resulting in an optimal failure rate of 0 by design. Methods in gray perform no face detection and are thus reported with additional supervision from bounding boxes generated with the ground truth landmarks. RGB datasets are indicated by [†].

pose, and background temperature (see Figure 4). The dataset is annotated with either 72 2D landmarks for frontal images or 43 2D landmarks for lateral images. The 43-point landmarks represent the visible landmarks in profile pictures with our information on orientation. We use a total of 7684 annotated frames with different resolutions with a minimal one of around 70x60 from the dataset. For evaluation, we propose to split the CHARLOTTE dataset based on image size and perspective. The High condition contains all images larger than the median image width of 200 pixels and Low all smaller images. The condition Side includes all images with profile annotations (43 landmarks), and Front contains all frontal faces (73 landmarks). In addition, we evaluate on the established RGB landmark dataset 300W [57] to verify RGB landmark prediction performance. It uses the classical 68-point convention. Here, we crop images to the pre-defined bounding boxes around each face for our evaluation. We follow the protocol from [64] for 300W evaluation. Average image resolution is about 290 pixels.

5.3. Comparison for Landmarking

We compare the landmarker performance with training on our full synthetic datasets against pre-trained models on the CHARLOTTE dataset. Besides relevant thermal landmarkers we include state-of-the-art RGB landmarkers. Thermal

Model	FID ↓	TUFTS MSE [47] ↓	DRIVE-IN MSE [13] ↓
Pix2Pix [25]	.2003	.0421	.1453
CycleGAN [65]	.2228	.0521	.0730
CUT [48]	.2140	.0468	.1370
QS-Attn [22]	.1173	.0409	.1303
$\lambda_R = 0, \lambda_W = 0$.5028	.0378	.1117
$\lambda_R = 0, \lambda_W = 0.01C$.3146	.0360	.1021
$\lambda_R = 1, \lambda_W = 0$.1706	<u>.0357</u>	.0545
$\lambda_R = 1, \lambda_W = 0.01C$	<u>.1598</u>	.0353	<u>.0580</u>

Table 3. Comparison to other models and regularizer influence on the thermalization. The parameter λ_W corresponds to the impact of the patch-based regularizer (Eq. (2)) and λ_R corresponds to the segmentation-based regularizer (Eq. (3)). We use $C = (5 \cdot 8^2)^{-1}$. The best value is in bold and the second-best is underlined.

performance of RGB landmarks can be boosted by applying a stack of unlearned linear filters before prediction [13]. Consequently, such pre-processing allows for a fairer comparison between task-specific thermal landmarks and RGB landmarks. We use label adaptation for all methods to account for different landmark conventions for the image evaluation. We train each label adaptation model with a 1000-image training split on CHARLOTTE similar to [60] and exclude the training split from the final evaluation. Note that this approach allows us to include our sparse model and our dense model in the evaluation. To benchmark the RGB performance of the multimodal model, we evaluate

Method	Training Data	300W (NME IO ↓)		
		Full	Comm.	Chal.
Star [64]	300W	0.0287	0.0252	0.0430
<i>Mediapipe</i> [39]	<i>undisclosed</i>	0.0562	0.0469	0.0947
FA [6]	LS3D-W	0.0435	0.0380	0.0661
<i>GLL+SW</i> ($\bar{\sigma} < \infty$)	FAKE	0.0570	0.0494	0.0874
<i>GLL+SW</i> ($\bar{\sigma} < \infty$)	FAKE + T-FAKE	0.0522	0.0468	0.0743

Table 4. Comparison of RGB performance. Label adaptation is trained on the 300W train split. Each method is evaluated on the 300W test split [23, 64]. For Star, we use the authors’ model pre-trained on 300W. NME has been normalized with the interocular distance [57, 60]. Methods with label adaptation are put in italic. Note that training with FAKE + T-FAKE does not degrade performance on 300W compared to FAKE alone.

our sparse model predictions against state-of-the-art RGB sparse landmarks on the 300W dataset.

CHARLOTTE performance. The NMEs and the failure rates of the different landmarks vary drastically for the CHARLOTTE splits with generally worse performance for the Front and Low conditions. As for the landmarks, we observe a clear advantage of GLL+SW ($\bar{\sigma} < \infty$) trained on FAKE+T-FAKE over GLL+SW ($\bar{\sigma} < \infty$) trained on FAKE only across sparse and dense landmarks, metrics, and splits. This confirms the suitability of our T-FAKE dataset for thermal landmarking. The FA and Mediapipe RGB landmarks and the SF-TL54 and Aachen thermal landmarks show comparable performance. Using a pre-processing stack [13], leads to a drastic failure reduction for the RGB landmarks. Our T-FAKE model achieves state-of-the-art performance for sparse thermal landmarking across all different conditions. The only models with comparable performance are Star which, however, performs no face detection and is evaluated with ground truth bounding boxes, and the TFW model which, however, only predicts a set of 5 landmarks. While the NME of the TFW model is slightly lower than our model for $\bar{\sigma} < \infty$ for Low, Front, and Full, our model outperforms Star and TFW on almost all dataset splits in terms of NME and failure rate for $\bar{\sigma} < 6 \times 10^{-4}$. These results are presented in Table 2 and examples are visualized in Figure 4. The 300W-trained RGB methods Star and 3FabRec use ground truth information for tight bounding box computation. Integration of face detection into their evaluation would presumably decrease the reported NMEs.

300W performance. We evaluate the RGB performance of our multimodal model on the 300W dataset in Table 4. Our model, trained on a combination of thermal and RGB facial images, with label adaptation performs between Mediapipe and FA with label adaptation. All methods are outperformed by Star. Note that Star is the only method trained on 300W landmarks and bounding boxes. Our implementation is the only one trained on general facial images and not on bounding boxes. Most importantly, training with FAKE only does not improve RGB performance.

5.4. Comparison for Thermalization

Our approach aims to overcome the limitations of thermal datasets to fixed camera angles, controlled lighting, and stable temperatures. However, this data limitation hinders the evaluation of ‘in-the-wild’ images. Therefore, we report three different metrics. Firstly, we report the average *Fréchet Inception Distance* (FID) [20] between all available thermal SEJONG images and five different equally-sized thermalized FAKE subsets. The FID measures perceptual quality without ground truth image pairs. Here, it compares the perceptual similarity of the thermal SEJONG dataset and thermalized FAKE datasets. Also, we report the mean-squared error (MSE) for two paired thermal datasets (with filtered background) to evaluate actual out-of-distribution temperature prediction. Here, we use TUFTS [47] and 1000 randomly selected images from DRIVE-IN [13]. TUFTS features frontal lab-condition images and DRIVE-IN contains side views from people in cars. Table 3 compares our final model ($\lambda_R = 1$, $\lambda_W = 0.01C$) to two supervised models trained with SEJONG only, a baseline implementation ($\lambda_R = 0$, $\lambda_W = 0$) and a Pix2Pix model [25], and three unsupervised models trained with SEJONG and FAKE, namely CycleGAN [65], CUT [48] and QS-Attn [22]. Our model outperforms all other models for temperature prediction and displays domain adaptation for the out-of-distribution DRIVE-IN data recorded outside a lab. Moreover, the resulting T-FAKE images display better perceptual similarity than all other methods except for QS-Attn. However, QS-Attn fails at temperature prediction, especially for the non-frontal DRIVE-IN images.

5.5. Thermalization Ablation Study

As an additional ablation of our regularizers, Table 3 presents FID and MSE for varied λ_W and λ_T . The segmentation-based regularizer leads to a large boost in perceptual similarity and temperature prediction power. The patch-based regularizer leads to a smaller boost. Combining both regularizers always gives the best or second-best result confirming the effectiveness of our RGB2Thermal loss.

6. Conclusion

Overcoming thermal data limitations, we established semi-supervised RGB2Thermal image translation. Using patch-based and segmentation-based regularization, we ensured thermalizer generalization to the synthetic FAKE dataset. This model generated the up-to-date largest thermal landmarking and segmentation dataset, the T-FAKE dataset. Using T-FAKE, we established the up-to-date first dense thermal landmarker and a state-of-the-art RGB+Thermal sparse landmarker. We performed strict landmarker benchmarking based on established thermal and RGB methods. Moreover, the underlying RGB2Thermal model displays excellent perceptual and temperature prediction performance.

7. Acknowledgements

This study has partially been funded by the Federal Ministry of Education and Research (BMBF, grant numbers 13N15753 and 13N15754). M.P. acknowledges funding from the German Research Foundation (DFG) within the GRK2260 BIOQIC project 289347353. The authors acknowledge HPC resources support with hardware funded by the DFG within project 469073465. The authors would like to thank Daniel J. Strauss for discussions and Mayur Bhamborae and Pascal Hirsch for technical support.

References

- [1] Fabian Altekrüger, Alexander Denker, Paul Hagemann, Johannes Hertrich, Peter Maass, and Gabriele Steidl. PatchNR: Learning from very few images by patch normalizing flow regularization. *Inverse Problems*, 39(6):064006, 2023. 4
- [2] Fabian Altekrüger and Johannes Hertrich. WPPNets and WPPFlows: The power of Wasserstein patch priors for super-resolution. *SIAM Journal on Imaging Sciences*, 16(3):1033–1067, 2023. 4
- [3] Roshanak Ashrafi, Mona Azarbayjani, and Hamed Tabkhi. Charlotte-ThermalFace: A fully annotated thermal infrared face dataset with various environmental conditions and distances. *Infrared Physics and Technology*, 124:104209, 2022. 1, 2, 3, 4, 5, 6, 12, 16, 17
- [4] D. Bitar, A. Goubar, and J.-C. Desenclos. International travels and fever screening during epidemics: A literature review on the effectiveness and potential use of non-contact infrared thermometers. *European communicable disease bulletin*, 14(6):19115, 2009. 1
- [5] Bjoern Browatzki and Christian Wallraven. 3fabrec: Fast few-shot face alignment by reconstruction. In *CVPR*, 2020. 7
- [6] Adrian Bulat and Georgios Tzimiropoulos. How far are we from solving the 2d & 3d face alignment problem? (and a dataset of 230,000 3d facial landmarks). In *CVPR*, pages 1021–1030, 2017. 2, 7, 8
- [7] Usman Cheema and Seungbin Moon. Sejong face database: A multi-modal disguise face database. *Computer Vision and Image Understanding*, 208:103218, 2021. 3, 12
- [8] Andrija Čosić, Igor Jovanović, Ivana Kostić, Miona Andrejević-Stošović, Dragan Krasić, and Dragan Mančić. Temperatures of different face regions of healthy people measured by a thermal camera. *Serbian Journal of Electrical Engineering*, 19(1):33–43, 2022. 4
- [9] Marco Cuturi. Sinkhorn distances: Lightspeed computation of optimal transport. *NIPS*, 26, 2013. 4
- [10] Jia Deng, Wei Dong, Richard Socher, Li-Jia Li, Kai Li, and Li Fei-Fei. Imagenet: A large-scale hierarchical image database. In *CVPR*, pages 248–255. IEEE, 2009. 12
- [11] Jiankang Deng, Anastasios Roussos, Grigorios Chrysos, Evangelos Ververas, Irene Kotsia, Jie Shen, and Stefanos Zafeiriou. The Menpo benchmark for multi-pose 2d and 3d facial landmark localisation and tracking. *International Journal of Computer Vision*, 127:599–624, 2019. 2
- [12] Jean Feydy, Thibault SÉjourné, François-Xavier Vialard, Shun-ichi Amari, Alain Trounev, and Gabriel Peyré. Interpolating between optimal transport and MMD using Sinkhorn divergences. In *AISTATS*, pages 2681–2690. PMLR, 2019. 4, 12
- [13] Philipp Flotho, Mayur J Bhamborae, Tobias Grün, Carlos Trenado, David Thinnies, Dominik Limbach, and Daniel J Strauss. Multimodal data acquisition at sars-cov-2 drive through screening centers: Setup description and experiences in saarland, germany. *Journal of Biophotonics*, 14(8):e202000512, 2021. 1, 2, 3, 4, 5, 7, 8, 12, 13, 16
- [14] P. Flotho, C. Heiss, G. Steidl, and D.J. Strauss. Lagrangian motion magnification with double sparse optical flow decomposition. *Frontiers in Applied Mathematics and Statistics*, 9:1164491, 2023. 1
- [15] Philipp Flotho, Cosmas Heiß, Gabriele Steidl, and Daniel J Strauss. Lagrangian motion magnification with landmark-prior and sparse pca for facial microexpressions and micro-movements. In *Annual International Conference of the IEEE Engineering in Medicine & Biology Society*, pages 2215–2218. IEEE, 2022. 1
- [16] V. Fomin, J. Anmol, S. Desroziers, J. Kriss, and A. Tejani. High-level library to help with training neural networks in pytorch. <https://github.com/pytorch/ignite>, 2020. 14
- [17] M. Godi, C. Joppi, A. Giachetti, F. Pellacini, and M. Cristani. Texel-att: Representing and classifying element-based textures by attributes. In *BMVC*, 2019. 14, 15
- [18] Ralph Gross, Iain Matthews, Jeffrey Cohn, Takeo Kanade, and Simon Baker. Multi-pie. *Image and Vision Computing*, 28(5):807–813, 2010. 2
- [19] Johannes Hertrich, Antoine Houdard, and Claudia Redenbach. Wasserstein patch prior for image superresolution. *IEEE Transactions on Computational Imaging*, 8:693–704, 2022. 4
- [20] Martin Heusel, Hubert Ramsauer, Thomas Unterthiner, Bernhard Nessler, and Sepp Hochreiter. Gans trained by a two time-scale update rule converge to a local Nash equilibrium. *NIPS*, 30, 2017. 8, 13
- [21] T.-H. Ho, C.-Y. Yu, T.-Y. Ko, and W.-T. Chu. The NCKU-VTF Dataset and a multi-scale thermal-to-visible face synthesis system. In *International Conference on Multimedia Modeling*, pages 463–475. Springer, 2023. 1, 3, 5
- [22] Xueqi Hu, Xinyue Zhou, Qiusheng Huang, Zhengyi Shi, Li Sun, and Qingli Li. Qs-attn: Query-selected attention for contrastive learning in i2i translation. In *CVPR*, pages 18291–18300, 2022. 7, 8, 13
- [23] Yangyu Huang, Hao Yang, Chong Li, Jongyoo Kim, and Fangyun Wei. Adnet: Leveraging error-bias towards normal direction in face alignment. In *Proceedings of the IEEE/CVF International Conference on Computer Vision*, pages 3080–3090, 2021. 8
- [24] Stephanos Ioannou, Vittorio Gallese, and Arcangelo Merla. Thermal infrared imaging in psychophysiology: potentialities and limits. *Psychophysiology*, 51(10):951–963, 2014. 1
- [25] Phillip Isola, Jun-Yan Zhu, Tinghui Zhou, and Alexei A Efros. Image-to-image translation with conditional adversarial networks. In *CVPR*, pages 1125–1134, 2017. 4, 7, 8, 13, 16
- [26] Justin Johnson, Alexandre Alahi, and Li Fei-Fei. Perceptual losses for real-time style transfer and super-resolution. In

- EECV*, pages 694–711. Springer, 2016. 16
- [27] V. Kazemi and J. Sullivan. One millisecond face alignment with an ensemble of regression trees. In *CVPR Workshops*, pages 1867–1874, 2014. 2
- [28] Ira Kemelmacher-Shlizerman, Steven M Seitz, Daniel Miller, and Evan Brossard. The MegaFace benchmark: 1 million faces for recognition at scale. In *CVPR*, pages 4873–4882, 2016. 1
- [29] Davis E. King. Dlib-ml: A machine learning toolkit. *Journal of Machine Learning Research*, 10:1755–1758, 2009. 2
- [30] Vladimir V Kniaz, Vladimir A Knyaz, Jiri Hladuvka, Walter G Kropatsch, and Vladimir Mizginov. Thermalgan: Multimodal color-to-thermal image translation for person re-identification in multispectral dataset. In *ECCV Workshops*, 2018. 3, 5
- [31] Martin Koestinger, Paul Wohlhart, Peter M Roth, and Horst Bischof. Annotated facial landmarks in the wild: A large-scale, real-world database for facial landmark localization. In *ICCV Workshops*, pages 2144–2151. IEEE, 2011. 2
- [32] Marcin Kopaczka, Lukas Breuer, Justus Schock, and Dorit Merhof. A modular system for detection, tracking and analysis of human faces in thermal infrared recordings. *Sensors*, 19(19):4135, 2019. 7
- [33] Marcin Kopaczka, Raphael Kolk, Justus Schock, Felix Burkhard, and Dorit Merhof. A thermal infrared face database with facial landmarks and emotion labels. *IEEE Transactions on Instrumentation and Measurement*, 68(5):1389–1401, 2018. 1, 2, 3, 4, 5, 7
- [34] M. Kowalski, J. Naruniec, and T. Trzcinski. Deep alignment network: A convolutional neural network for robust face alignment. In *CVPR Workshops*, pages 88–97, 2017. 2
- [35] Abhinav Kumar, Tim K Marks, Wenxuan Mou, Ye Wang, Michael Jones, Anoop Cherian, Toshiaki Koike-Akino, Xiaoming Liu, and Chen Feng. Luvli face alignment: Estimating landmarks’ location, uncertainty, and visibility likelihood. In *CVPR*, pages 8236–8246, 2020. 2
- [36] Askat Kuzdeuov, Dana Aubakirova, Darina Koishigarina, and Huseyin Atakan Varol. Tfw: Annotated thermal faces in the wild dataset. *IEEE TIFS*, 17:2084–2094, 2022. 2, 3, 4, 5, 7, 16
- [37] A. Kuzdeuov, D. Koishigarina, D. Aubakirova, S. Abushakimova, and H. A. Varol. Sf-tl54: A thermal facial landmark dataset with visual pairs. In *IEEE/SICE International Symposium on System Integration*, pages 748–753. IEEE, 2022. 2, 3, 4, 5, 7
- [38] Arthur Leclaire and Julien Rabin. A stochastic multi-layer algorithm for semi-discrete optimal transport with applications to texture synthesis and style transfer. *Journal of Mathematical Imaging and Vision*, 63(2):282–308, 2021. 4
- [39] Camillo Lugaresi, Jiuqiang Tang, Hadon Nash, Chris McClanahan, Esha Uboweja, Michael Hays, Fan Zhang, Chuoling Chang, Ming Yong, Juhyun Lee, et al. Mediapipe: A framework for perceiving and processing reality. In *CVPR Workshops*, 2019. 1, 5, 6, 7, 8, 16
- [40] Khawla Mallat and Jean-Luc Dugelay. A benchmark database of visible and thermal paired face images across multiple variations. In *International Conference of the Biometrics Special Interest Group*, pages 1–5. IEEE, 2018. 3
- [41] Khawla Mallat and Jean-Luc Dugelay. Facial landmark detection on thermal data via fully annotated visible-to-thermal data synthesis. In *IJCB*, pages 1–10. IEEE, 2020. 1, 2, 3, 5
- [42] Osama Mazhar and Jens Kober. Random shadows and highlights: A new data augmentation method for extreme lighting conditions. *arXiv preprint arXiv:2101.05361*, 2021. 12
- [43] Pietro Melzi, Ruben Tolosana, Ruben Vera-Rodriguez, Minchul Kim, Christian Rathgeb, Xiaoming Liu, Ivan DeAndres-Tame, Aythami Morales, Julian Fierrez, Javier Ortega-Garcia, et al. Frcsyn-ongoing: Benchmarking and comprehensive evaluation of real and synthetic data to improve face recognition systems. *Information Fusion*, 107:102322, 2024. 2
- [44] Nithin Gopalakrishnan Nair and Vishal M Patel. T2v-ddpm: Thermal to visible face translation using denoising diffusion probabilistic models. In *International Conference on Automatic Face and Gesture Recognition*, pages 1–7. IEEE, 2023. 3, 5, 12
- [45] E. Y.-K. Ng. Is thermal scanner losing its bite in mass screening of fever due to sars? *Medical Physics*, 32(1):93–97, 2005. 1
- [46] Roman Novak, Yasaman Bahri, Daniel A Abolafia, Jeffrey Pennington, and Jascha Sohl-Dickstein. Sensitivity and generalization in neural networks: an empirical study. In *ICLR*, 2018. 12
- [47] Karen Panetta, Qianwen Wan, Sos Agaian, Srijith Rajeev, Shreyas Kamath, Rahul Rajendran, Shishir Paramathma Rao, Aleksandra Kaszowska, Holly A Taylor, Arash Samani, et al. A comprehensive database for benchmarking imaging systems. *IEEE Transactions on Pattern Analysis and Machine Intelligence*, 42(3):509–520, 2018. 7, 8, 12, 13
- [48] Taesung Park, Alexei A Efros, Richard Zhang, and Jun-Yan Zhu. Contrastive learning for unpaired image-to-image translation. In *EECV*, pages 319–345. Springer, 2020. 7, 8, 13
- [49] M. Piening, F. Altekrieger, J. Hertrich, P. Hagemann, A. Walther, and G. Steidl. Learning from small data sets: Patch-based regularizers in inverse problems for image reconstruction. *arXiv preprint arXiv:2312.16611*, 2023. 4
- [50] Domenick Poster, Shuowen Hu, Nasser Nasrabadi, and Benjamin Riggan. An examination of deep-learning based landmark detection methods on thermal face imagery. In *CVPR Workshops*, pages 0–0, 2019. 1
- [51] Domenick Poster, Matthew Thielke, Robert Nguyen, Sriniwasan Rajaraman, Xing Di, Cedric Nimpa Fondje, Vishal M Patel, Nathaniel J Short, Benjamin S Riggan, Nasser M Nasrabadi, et al. A large-scale, time-synchronized visible and thermal face dataset. In *WACV*, pages 1559–1568, 2021. 1, 2, 3, 4, 5
- [52] Domenick D Poster, Shuowen Hu, Nathan J Short, Benjamin S Riggan, and Nasser M Nasrabadi. Visible-to-thermal transfer learning for facial landmark detection. *IEEE Access*, 9:52759–52772, 2021. 3, 16
- [53] B. J. Quilty, S. Clifford, S. Flasche, R. M. Eggo, et al. Effectiveness of airport screening at detecting travellers infected with novel coronavirus (2019-ncov). *European communicable disease bulletin*, 25(5):2000080, 2020. 1
- [54] Md Shohel Rana, Mohammad Nur Nobil, Beddhu Murali, and Andrew H Sung. Deepfake detection: A systematic literature review. *IEEE Access*, 10:25494–25513, 2022. 1

- [55] Benjamin S Riggan, Nathaniel J Short, and Shuowen Hu. Thermal to visible synthesis of face images using multiple regions. In *WACV*, pages 30–38. IEEE, 2018. [3](#), [12](#)
- [56] Olaf Ronneberger, Philipp Fischer, and Thomas Brox. U-net: Convolutional networks for biomedical image segmentation. In *MICCAI*, pages 234–241. Springer, 2015. [4](#)
- [57] Christos Sagonas, Epameinondas Antonakos, Georgios Tzimiropoulos, Stefanos Zafeiriou, and Maja Pantic. 300 faces in-the-wild challenge: Database and results. *Image and Vision Computing*, 47:3–18, 2016. [1](#), [2](#), [6](#), [7](#), [8](#)
- [58] Mark Sandler, Andrew Howard, Menglong Zhu, Andrey Zhmoginov, and Liang-Chieh Chen. Mobilenetv2: Inverted residuals and linear bottlenecks. In *CVPR*, pages 4510–4520, 2018. [5](#)
- [59] Saurabh Sonkusare, Michael Breakspear, Tianji Pang, Vinh Thai Nguyen, Sascha Frydman, Christine Cong Guo, and Matthew J Aburn. Data-driven analysis of facial thermal responses and multimodal physiological consistency among subjects. *Scientific Reports*, 11(1):12059, 2021. [4](#)
- [60] Erroll Wood, Tadas Baltrušaitis, Charlie Hewitt, Sebastian Dziadzio, Thomas J Cashman, and Jamie Shotton. Fake it till you make it: face analysis in the wild using synthetic data alone. In *ICCV*, pages 3681–3691, 2021. [1](#), [2](#), [3](#), [5](#), [6](#), [7](#), [8](#), [15](#), [16](#)
- [61] Erroll Wood, Tadas Baltrušaitis, Charlie Hewitt, Matthew Johnson, Jingjing Shen, Nikola Milosavljevic, Daniel Wilde, Stephan Garbin, Toby Sharp, Ivan Stojiljkovic, Tom Cashman, and Julien Valentin. 3d face reconstruction with dense landmarks. In *ECCV*, 2022. [1](#), [2](#), [5](#), [7](#), [15](#), [16](#), [17](#)
- [62] H. Zhang, B. S. Riggan, S. Hu, N. J. Short, and V. M. Patel. Synthesis of high-quality visible faces from polarimetric thermal faces using generative adversarial networks. *International Journal of Computer Vision*, 127:845–862, 2019. [3](#), [4](#), [5](#)
- [63] Teng Zhang, Arnold Wiliem, Siqi Yang, and Brian Lovell. Tv-gan: Generative adversarial network based thermal to visible face recognition. In *International Conference on Biometrics*, pages 174–181. IEEE, 2018. [3](#), [5](#), [12](#), [16](#)
- [64] Zhenglin Zhou, Huaxia Li, Hong Liu, Nanyang Wang, Gang Yu, and Rongrong Ji. Star loss: Reducing semantic ambiguity in facial landmark detection. In *Proceedings of the IEEE/CVF conference on computer vision and pattern recognition*, pages 15475–15484, 2023. [7](#), [8](#)
- [65] Jun-Yan Zhu, Taesung Park, Phillip Isola, and Alexei A Efros. Unpaired image-to-image translation using cycle-consistent adversarial networks. In *ICCV*, pages 2223–2232, 2017. [7](#), [8](#), [13](#)
- [66] Xiangyu Zhu, Xiaoming Liu, Zhen Lei, and Stan Z Li. Face alignment in full pose range: A 3d total solution. *IEEE Transactions on Pattern Analysis and Machine Intelligence*, 41(1):78–92, 2017. [2](#)
- [67] Xiangxin Zhu and Deva Ramanan. Face detection, pose estimation, and landmark localization in the wild. In *CVPR*, pages 2879–2886. IEEE, 2012. [6](#)

Supplementary Material

In the supplementary material, we give additional information for our method. In Section A we provide more details on the thermalization including implementation details and an extended ablation study. In Section B, we add details on landmarker and label adaptation implementation. In Sections C-E we discuss limitations and provide additional result images of the datasets.

A. Thermalization

A.1. Reference Temperature Values

As described in the main document, we train two versions of the thermalizer T_θ to model facial temperature variations under different environmental conditions. For that purpose, we use two sets of reference temperatures, a ‘cold’ and a ‘warm’ condition, for the different facial regions that guide the segmentation-based regularizer. These are presented in Table 5. Thermal facial contrast is increased and overall body temperature is decreased for the ‘cold’ condition in comparison to the ‘warm’ condition which is in line with empirical findings [3].

Segmentation	‘Cold’	‘Warm’
Background, Glasses	<20	<20
Skin	33	35
Nose	31.5	35
Eyes	34	35
Brows	31	34
Ears	32	35
Mouth Interior	35	35
Lips	32.5	35
Neck	34	35
Hair	30	30
Beard	31	32
Clothing	30	32
Headwear, Facewear	28	28

Table 5. Reference temperatures in Celsius for our segmentation-based regularizer for the ‘cold’ and the ‘warm’ setup. Note that our pixel range goes from 20 °C to 40 °C.

A.2. Thermalization Implementation Details

For the patch-based regularizers, we use random batches with patch size of 8. We disregard the background by excluding synthetic patches based on the ground truth background segmentation and completely black real patches. For our multi-scale approach, we sum the regularizer over 5 scales with a downsampling factor of 0.5. Again, facial temperatures depend on the surrounding temperature. Thus, we train a ‘warm’ and a ‘cold’ model with different reference temperature values for the segmentation-based regularizers. For data augmentation, we use the same random rotations and cropping for the natural RGB and thermal images. Moreover, we apply random color changes, blurring, and shadow augmentations [42] exclusively to the natural RGB images. Next, we apply random rotations and cropping for the synthetic RGB images. Here, we also fill holes in the original ‘glasses’ segmentation

masks showing outlines of the frame only to highlight transparent, but heat-blocking glass or plastic. Lastly, we replace the original background with a black background based on the known semantic segmentation. We use a U-Net T_θ with a Resnet34 encoder pre-trained on ImageNet [10] and train it for 10 FAKE epochs with SEJONG batches of size 64 and FAKE batches of size 64. This corresponds to approximately 100 SEJONG epochs. Further, we use an Adam optimizer with an initial learning rate of 0.001 which we reduce to 0.0001 after 4 epochs. Based on a random split, we use 80% of the SEJONG data for training and all available FAKE data. Also, we use the *geomloss* [12] implementation for the Wasserstein patch loss with $\lambda_E = 0.1^6$. We normalize the squared error loss $\|\cdot - \cdot\|_2^2$ by dividing with the image dimension, here 256^2 . Based on the 5 scales and patch dimension 8^2 , we set $\lambda_W = 0.01C$ for our final model with the normalization constant $C = (5 \cdot 8^2)^{-1}$. We set $\lambda_R = 1$. Note that the choice of $\lambda_R = 1$ and C are motivated to control the value range. The (normalized) MSE data fidelity term $\|\cdot - \cdot\|_2^2$ which we evaluate on normalized SEJONG images takes values in the range $[0, 1]$ for arbitrary images with pixel range $[0, 1]$ due to dimensional normalization. To have a similar value range for the evaluated FAKE images, the patch-based regularizer W takes values in $[0, 1]$ for $\lambda_W = C$ with arbitrary normalized images. Moreover, the segmentation-based regularizer R also takes values in $[0, 1]$ for such images given arbitrary normalized reference temperature values in $[0, 1]$ for $\lambda_R = 1$.

A.3. SEJONG Dataset

The SEJONG dataset illustrates the impact of various disguises, including glasses, wigs, and fake beards. Each subject in the dataset is presented with different disguises. As a result, it includes a lot of clothing and hairstyle variations. Most participants have a Southeast Asian or Central Asian ethnic background, but people of other ethnicities are included too. The number of participants identifying as male or female is balanced. This makes it an attractive dataset candidate for thermalization training that is supposed to generalize to a large variety of subjects. Due to reasons of data privacy, we refer to the original publication [7] and have to abstain from showing additional SEJONG images.

A.4. Generalization to Out-of-Lab Conditions

The success of neural networks in the last two decades has been tremendous, especially in the imaging domain. Nevertheless, a common empirical finding is the limited capability of neural networks to generalize to new settings [46]. Often, this limitation is caused by biased datasets. Particularly in the biomedical domain, data acquisition is a valuable task. However, due to real-world restrictions, data is often acquired in laboratory conditions. Acquiring paired RGB and thermal facial images requires a calibrated multimodal camera setup. Most multimodal facial datasets are restricted to frontal views with relatively neutral expressions and frontal lighting, e.g. [7, 13, 47]. As a direct consequence, most Thermal2RGB research has focused on learning the transformation purely for *frontal images with frontal lighting at room temperature* [44, 55, 63]. To our knowledge, our regularized model is the first facial model to promote the explicit generalization of a learned thermal transformation to new poses, facial expressions, and lighting conditions and to simulate distinct temperature conditions. However, due to a lack of paired multimodal ‘in-the-wild’



Figure 5. Thermalization results for *frontal* RGB images with paired thermal images from the TUFTS [47] database without regularization ($\lambda_W = 0, \lambda_R = 0$), Pix2Pix and our final model ($\lambda_W = 0.001C, \lambda_R = 1$) (top to bottom).

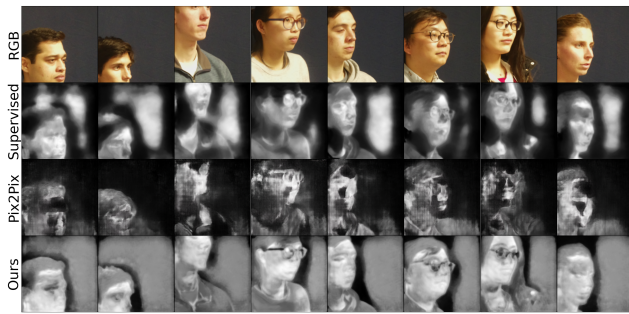


Figure 6. Thermalization results for *side* RGB images without paired thermal images from the TUFTS [47] database without regularization ($\lambda_W = 0, \lambda_R = 0$), Pix2Pix and our final model ($\lambda_W = 0.001C, \lambda_R = 1$) (top to bottom).

facial datasets, we have to partially resort to metrics for unsupervised image translation, i.e., the FID [20]. To additionally visualize this result, we show results for the TUFTS [47] dataset containing RGB and thermal images. Again, we find that paired RGB and images are only available for frontal views. We present the results of applying our baseline model without regularization ($\lambda_W = 0, \lambda_R = 0$), a Pix2Pix model, and our final ‘cold’ model to the dataset subset with paired RGB images in Figure 5. We chose the ‘cold’ model because the images were recorded at room temperature. We see only a marginal impact of our regularization on the prediction. However, the TUFTS dataset additionally contains RGB images without paired thermal images recorded from different angles. Therefore, we also apply both models to random images taken from a fixed side angle. The result is displayed in Figure 6. We see that the unregularized model generates various large facial artifacts whereas our final model contains almost no facial artifacts. This shows that the main limitation of training RGB2Thermal and Thermal2RGB models is the lack of paired ‘in-the-wild’ multimodal images. Our regularization allows us to overcome this limitation.



Figure 7. Comparison of FAKE images thermalized with Pix2Pix [25], CycleGAN [65], CUT [48], QS-Attn [22], our supervised baseline and our final model (top to bottom, background removed).



Figure 8. Thermal ground truth samples from the DRIVE-IN [13] dataset with side profile.

A.5. Thermalization Comparison Details

We used the official PyTorch implementation for all compared models. We trained Pix2Pix and all SEJONG images and all unsupervised images using all $\sim 10k$ SEJONG images and 10k FAKE (RGB) images. We used default hyperparameters and trained all models for 10 epochs with a constant learning rate and an additional 10 epochs with a linearly decreasing learning rate. All models were trained and evaluated with a resolution of 256 for the FID and the MSE. However, our models were evaluated on a resolution of 512 and the output was downscaled to 256 to be in line with the final T-FAKE dataset. We display examples in Figure 7. For the MSE comparison, we removed the background because we use random background augmentations for our final landmarker training. Here, we removed the background by masking all predictions based on a 21°C threshold based on the ground truth. For the FID evaluation, we randomly choose the ‘warm’ or the ‘cold’ variant for each image for our model. For the MSE, we average the results for ‘warm’ and ‘cold’ variants. Due to data privacy reasons, we are only able to present ground truth thermal images for two persons from the DRIVE-IN dataset [13], see Figure 8.



Figure 9. T-Fake samples with original images (first row), ‘cold’ images’ (second row), and ‘warm’ images’ (third row). Note the diminished contrasts of the noses and the checks.

Regularization	$\lambda_R = 1$	$\lambda_R = 0$
$\lambda_W = 1C$	$.1665 \pm .0030$	$.3375 \pm .0056$
$\lambda_W = 0.1C$	$.1753 \pm .0018$	$.3654 \pm .0032$
$\lambda_W = 0.01C$	$.1598 \pm .0041$	$.3146 \pm .0092$
$\lambda_W = 0$	$.1706 \pm .0029$	$.5028 \pm .0054$

Table 6. Impact of the regularization parameters on the perceptual quality measured with the FID (\downarrow) with $C = (5 \cdot 8^2)^{-1}$.

A.6. Extended Thermalization Ablation Study

Given that the regularizers are solely defined for the synthetic images, we fix $\lambda_T = 1$ to ensure that the regularizer is on the same scale as the MSE of the real images and vary λ_W for our ablation. We train all models with the same setup and random seeds. The FID implementation is the default *PyTorch-Ignite* [16] implementation. Here, we extend the ablation study table in the main document which only displays the best result for $\lambda_W = 0.01C$. In particular, we display the results of a grid search for λ_W and λ_R in Table 6. As described in the main document, we calculate the mean FID and its standard deviation for five different subsets of the T-FAKE dataset. Moreover, we use the same setup to compare the perceptual quality of the ‘cold’ and the ‘warm’ setup of our final T-FAKE dataset, see Table 7. Figure 9 shows T-FAKE samples with the ‘cold’ and ‘warm’ variants. In addition, we present some samples generated with different regularization configurations in Figure 10 for the ‘cold’ setup and in Figure 11 for the ‘warm’ setup. Here, we can visually see the impact of the different regularizers.

According to the FID, both regularizers have a positive impact. The segmentation-based regularizer greatly boosts the perceptual quality, while the effect of the patch-based regularizer is smaller. The optimal FID value is obtained for $\lambda_W = 0.01C$ and $\lambda_T = 1$,

Setup	‘Cold’	‘Warm’
FID \downarrow	$.1577 \pm .0024$	$.1685 \pm .0111$

Table 7. Perceptual comparison of thermal setups ‘cold’ and ‘warm’ using the FID.



Figure 10. Regularization impact on images for ‘cold’ setup: No regularization ($\lambda_W = 0$, $\lambda_R = 0$), only patch-based ($\lambda_W = 0.01C$, $\lambda_R = 0$), only segmentation-based ($\lambda_W = 0$, $\lambda_R = 1$), and final model ($\lambda_W = 0.01C$, $\lambda_R = 1$) (top to bottom).

the parameters of our final model. The perceptual quality of the figures seems in line with the FID. A closer look at the last two rows in both figures shows that the segmentation-based regularizer alone can lead to smoothed facial areas and overly exaggerated differences on the edges of the semantic segmentation. This becomes more apparent for the ‘cold’ setup as it leads to more thermal contrast within the face, see Figure 10. The FID shows only a small difference between the ‘cold’ and ‘warm’ variants. The ‘warm’ variant displays slightly lower FID values. For a visual comparison of the T-FAKE images with real thermal images, we refer to Fig. 12.

B. Landmarking

B.1. CHARLOTTE Dataset

The CHARLOTTE dataset contains thermal images with varying thermal conditions, various head positions, and multiple camera distances. Moreover, it contains information about the thermal sensation of the subjects. We refer to Fig. 12 for a visualization of some thermal CHARLOTTE images without landmarks.

B.2. Landmarking Implementation Details

For training, we include random landmark positions on a texture dataset [17] as negative examples into the dataset to increase the

Metric	Method	Training Dataset	High	Low	Side	Front	Full
NME W/H ↓	GLL + RW ($\bar{\sigma} < \infty$) [60, 61]	FAKE	0.1055	0.2675	0.1241	0.2534	0.1887
	GLL + RW* ($\bar{\sigma} < \infty$)	FAKE	0.0933	0.2682	0.1312	0.2348	0.1824
	GLL + RW ($\bar{\sigma} < \infty$)	T-FAKE	0.0832	0.1334	0.0677	0.1503	0.1090
	GLL + RW ($\bar{\sigma} < \infty$)	FAKE + T-FAKE	0.0740	0.1346	0.0684	0.1420	0.1051

Table 8. Ablation results on CHARLOTTE dataset splits. Pre-processing with the pre-processing stack for RGB landmarks is indicated by *. The confidence threshold has been set to infinity. RGB + Thermal (FAKE + T-FAKE) and Thermal Only (T-FAKE) models have been finetuned from the FAKE models.



Figure 11. Regularization impact on images for ‘warm’ setup: No regularization ($\lambda_W = 0, \lambda_R = 0$), only patch-based ($\lambda_W = 0.01C, \lambda_R = 0$), only segmentation-based ($\lambda_W = 0, \lambda_R = 1$), and final model ($\lambda_W = 0.01C, \lambda_R = 1$) (top to bottom).

learned uncertainty σ^2 on images without faces. On thermal images, we fill in the background with random textures from the texture dataset [17] with a probability of 0.25. During inference, we use a multi-scale sliding window evaluation to generalize our model to varying image sizes and face scales. We downsample iteratively with a factor of 0.75 until the height or the width reaches 224. For each image scale, we run our model on sliding windows of size 224×224 with a stride of 20. For our final landmark prediction, we pool all predictions and use the landmark with the smallest predicted standard deviation across all scales and all sliding windows. For training the landmarker T_ψ , we finetune a model that has been pre-trained on the original FAKE dataset for the sparse landmarker for the results in Table 8. During refinement, thermal images are used with a probability of 0.4 split with equal probability for ‘cold’ and ‘warm’ conditions. We finetune for 100 epochs with a learning rate of 0.0004, Adam optimizer with weight decay, batchsize of 512 and OneCycleLR scheduler. Our final model is trained for 4000 epochs, a learning rate of 0.001 on FAKE and T-FAKE ($p=0.4$).



Figure 12. CHARLOTTE image samples with different resolutions, environmental conditions, and subjects.

Augmentations details. We use of spatial augmentations, including random shear, rotations, resizing, and cropping to allow the landmarker to learn a large variation of face orientations without the need for a dedicated face detector. Specifically, we use geometric augmentations which apply random rotations (up to $\pm 45^\circ$) and random shear ($\pm 7^\circ$) to both the image and landmarks, preserving geometric consistency. In addition, a random resized cropping operation is performed, with the cropped region size scaling between 40% and 200% of the original image and an aspect ratio ranging between $\frac{3}{4}$ and $\frac{4}{3}$. Furthermore, we use photometric transformations and random Gaussian smoothing. The thermal images are randomly jittered to simulate temperature variations and thermal images are randomly inverted with a probability of 0.1. Additionally, random noise is applied with a probability of 0.2 to simulate sensor noise. See Figure 17 for image examples with augmentations applied.

B.3. Label Adaptation Implementation Details

Label Adaptation was trained for each method on the predictions on all detected faces on a random 1000 image CHARLOTTE split. We train a model T_ζ for 2000 epochs with a learning rate 0.002,

OneCycleLR and Adam optimizer. As landmark augmentations, we apply random rotation up to 45° as well as random shearing during training. The label adaptation network is a five-layer perceptron with fully connected layers that takes the predicted landmarks together with the resize factor as input. The latter accounts for varying degrees of quantization at different image sizes in the CHARLOTTE ground truth. The label adaptation generally handles even outlier predictions but can also contain fail cases, (see Figure 14).

RGB Model Inference. We use two different pre-processing approaches to include landmarkers solely developed for RGB images into the evaluation. Firstly, gray-value images, where the temperature between 20° and 45° is normalized and, secondly the pre-processing stack proposed in [13]. The pre-processing stack consists of temperature clamping between 20°C and 45°C , unsharp masking with two sets of parameters with and without temperature inversion. The reported landmarks are the averages over all detected faces. This simple pre-processing stack is a simple method for boosting RGB landmarker performance for thermal images [13]. As a result, we can include RGB landmarkers as a baseline for thermal landmarking models.

B.4. Landmarking Ablation Study

To study the impact of our thermal data, we report the CHARLOTTE results of our landmarker trained with i) RGB images only, ii) finetuned with thermal images and iii) finetuned with both FAKE and T-FAKE. Again, we use label adaptation for all variations. Table 8 shows the results. Training with the T-FAKE dataset significantly improves the accuracy of thermal landmarking across all conditions. In addition, multimodal training with the FAKE and T-FAKE datasets leads to better thermal landmarking performance than finetuning only with the T-FAKE dataset.

B.5. Inference Ablation

We analyze the impact of our inference strategy, see Table 9. We compare inference on i.) the complete image scaled to 224×224 (whole image), ii.) followed by refinement on a bounding box computed from the predictions obtained with i.) and finally iii.) with the sliding window approach described in the main document. Method iii.) produces the best results over all images except for Charlotte low, where ii.) performs slightly better while at the same time being also suitable for real time estimation.

C. Large-Scale Visualization

For a large number of T-FAKE samples, we refer to Figures 15 and 16. Here, we simply use the first 128 images based on the numerical naming convention of the original FAKE dataset.

D. Thermal Semantic Segmentation Dataset

Note that by design detailed segmentation masks are available for all T-FAKE images. While the training of a semantic segmentation model was out-of-scope for our work, we want to highlight the fact that our dataset can also be used for such training. The possibility of such segmentation training with synthetic data has already been demonstrated by Wood et al. [60].

E. Limitations

Thermalization. This work depends on the thermalization of the final renders in the FAKE dataset. The dataset contains very difficult lighting conditions and scene compositions that make it powerful to train landmarkers but also made the thermalization particularly challenging and could only be solved with advanced domain-adaptive semi-supervised regularization approaches. Despite a good perceptual result of the faces, some T-FAKE images can contain minor artifacts on clothing and on the background (e.g. see Figure 11, bottom second from right). Nevertheless, these artifacts remain limited. Moreover, background artifacts can easily be removed by choosing a suitable background based on the ground truth segmentation as implemented during our landmarker training, see Fig. 17. We merely used an MSE loss for our supervised training. Including an adversarial [25, 63] or a perceptual [26, 52] loss into our model might lead to perceptual improvement.

Dense Landmarks. In this work, we relied on the ground truth 70-point landmarks of the FAKE dataset [60] and dense Mediapipe [39] annotations. Training with the original 320- and 702-point landmarks could further boost accuracy and lead to an even denser landmarker. However, these landmarks are not publicly available. Furthermore, we only evaluate a mobilenet backbone for landmark detection without face tracking. Better performance for difficult poses and face variability could be achieved with denser models [61] and spatial normalization of face positions during training.

CHARLOTTE. The CHARLOTTE [3] dataset is among the largest datasets with thermal recordings of faces that contain different levels of image quality as well as has a high variability in poses such as side profile pictures and tilting which makes the dataset ideal as a benchmark. However, the 2D annotation uses a convention where side profile images have a different number of landmarks than frontal faces. Furthermore, landmarks of low-resolution images are quantized and there are examples of shifted ground truth annotations (see Figure 13).

Label Adaptation. We retrain the label adaptation networks for each tested landmarker on its original predictions. Hence, for a given method, a high failure rate on CHARLOTTE means that fewer training images are available for that method. Also, poor predictions on some of the images such as profile images without failure produce a low quality of adapted landmarks (see Figure 14, TL54 dlib, column 3). It is important to note that the label adaptation does not use visual information from the benchmark dataset to translate landmarks. However, the same individuals were present in both the test and the training datasets which might allow networks to learn facial statistics of individuals. This might give an advantage to landmarkers with only a few landmarks, e.g., TFW [36] (see Figure 14, TFW). The good 68-point landmark performance of TFW on the CHARLOTTE dataset does not necessarily mean that this generalizes and the advantage of increasing the number of predicted landmarks has been demonstrated for RGB images [61].



Figure 13. Results on examples from the **CHARLOTTE** dataset [3] with different RGB and thermal predictors and our models. For images without landmarks, no faces were detected. The performance of RGB methods can be greatly improved when the images are inverted or sharpened indicated by *. The first column shows the limitations in the **CHARLOTTE** ground truth: profile annotation convention for frontal views (1st row), quantization artefacts for low resolution images (4th row), translated annotations (last row).

Method	Inference Time (ms)	High	Low	Side	Front	Full
Sliding window ($\bar{\sigma} < \infty$)	88.73	0.0740	0.1346	0.0684	0.1420	0.1051
Refined bounding box ($\bar{\sigma} < \infty$)	10.41	0.0847	0.1329	0.0696	0.1494	0.1095
Whole image ($\bar{\sigma} < \infty$)	5.92	0.1091	0.1868	0.0842	0.2139	0.1490

Table 9. NME (W/H) (\downarrow) for **CHARLOTTE** splits with different strategies for landmark computation. The final results are estimated with sliding windows similar to [61], however, we achieved comparable results when computing the landmarks on input images rescaled to 224×224 . Here, we do not exclude high-uncertainty images and evaluate all images without failure rate, i.e., $\bar{\sigma} < \infty$. Average inference time per frame on the Full split has been benchmarked on a single NVIDIA H100 80GB GPU with a batch size of 1.



Figure 14. Label adaptation examples. For side profile views in the CHARLOTTE dataset only landmarks for visible parts of the face exist and additional positions on the forehead are marked. Label adaptation translates the three different landmark conventions we use for evaluation (bottom) into the CHARLOTTE convention (top).

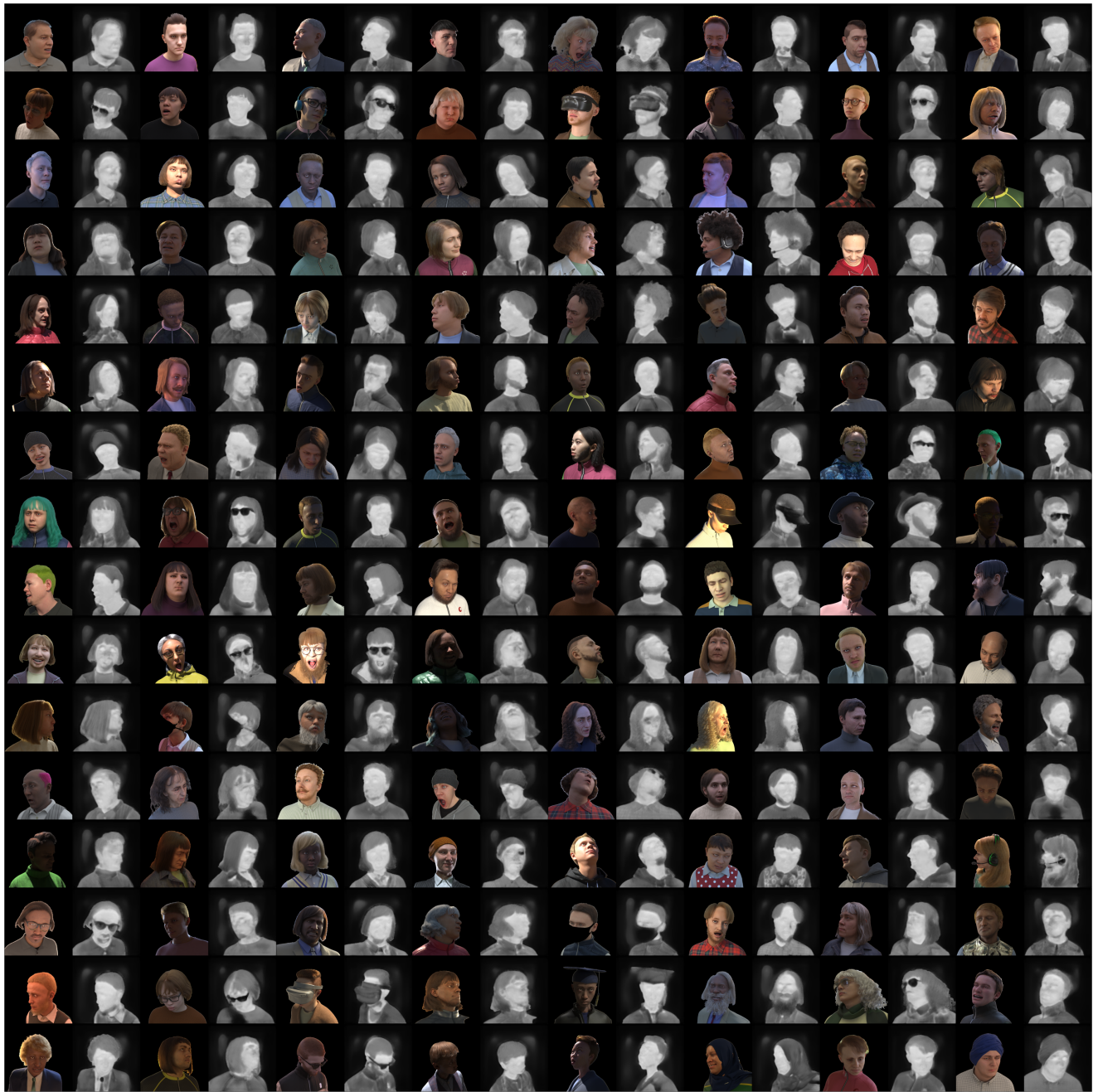


Figure 15. The first 128 FAKE (with removed background) and T-FAKE images with a random choice between the ‘cold’ and the ‘warm’ variant.



Figure 16. The sparse landmarks for the T-FAKE images in Fig. 15

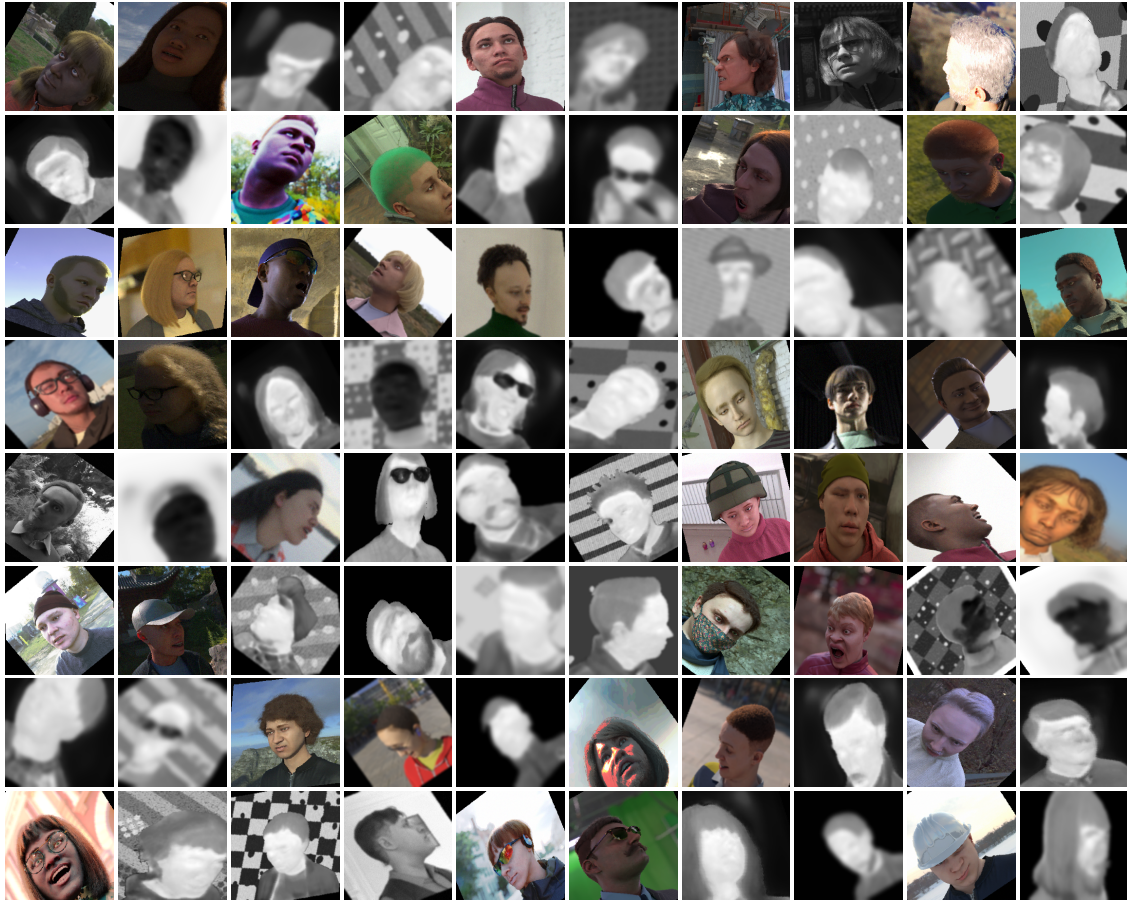


Figure 17. Example images from FAKE and T-FAKE with the augmentations applied during training.